FULL PAPER

Identifying the Conversion Mechanism of NiCo$_2$O$_4$ during Sodiation–Desodiation Cycling by In Situ TEM

Chongyang Zhu, Feng Xu,* Huihua Min, Yuan Huang, Weiwei Xia, Yuanting Wang, Qingyu Xu, Peng Gao,* and Litao Sun*

For alkali metal ion batteries, probing the ion storage mechanism (intercalation- or conversion-type) and concomitant phase evolution during sodiation–desodiation cycling is critical to gain insights into understanding how the electrode functions and thus how it can be improved. Here, by using in situ transmission electron microscopy, the whole sodiation–desodiation process of spinel NiCo$_2$O$_4$ nanorods is tracked in real time. Upon the first sodiation, a two-step conversion reaction mechanism has been revealed: NiCo$_2$O$_4$ is first converted into intermediate phases of CoO and NiO that are then further reduced to Co and Ni phases. Upon the first desodiation, Co and Ni cannot be recovered to original NiCo$_2$O$_4$ phase, and divalent metal oxides of CoO and NiO are identified as desodiated products for the first time. Such asymmetric conversion reactions account for the huge capacity loss during the first charging–discharging cycle of NiCo$_2$O$_4$-based sodium-ion batteries (SIBs). Impressively, a reversible and symmetric phase transformation between CoO/Co and NiO/Ni phases is established during subsequent sodiation–desodiation cycles. This work provides valuable insights into mechanistic understanding of phase evolution during sodiation–desodiation of NiCo$_2$O$_4$, with the hope of assistance in designing SIBs with improved performance.

1. Introduction

The ever-growing energy demand in electric vehicles and smart grids has inspired intensive studies in large-scale electric energy storage (EES) technologies beyond lithium-ion batteries (LIBs).[1–5] Among them, sodium-ion batteries (SIBs) have received great attention lately as an alternative to LIBs due to the high abundance and low cost of sodium resources.[6–10] To enable SIB technology, many host materials have been attempted so far as anode electrodes, including Sn, SnP$_3$, MoO$_2$, and Co$_9$S$_8$, etc.[11–15] However, it is still challenging for finding suitable SIBs electrode material, as sodium ions have a larger radius and heavier mass than those of lithium ions, which would significantly impact the ion transport and the reaction kinetics with electrodes.[16–18] Moreover, compared with rich research on LIBs, the science of SIBs is much less understood in most materials systems.

Recently, ternary metal oxides, especially NiCo$_2$O$_4$ materials, are considered as promising electrode materials in EES devices for their synergic effects of multiple metal species and the high capacity.[19–21] They exhibit higher electrical conductivity and electrochemical activities than single metal oxides by generating two active metallic components with relatively low activation energy for electron transfer.[22,23] These attractive features make NiCo$_2$O$_4$ have potential for SIBs. Alcántara et al. first proved that NiCo$_2$O$_4$ powder has the ability to store Na but delivered a poor reversible capacity and cycling performance.[24] To address these issues, various NiCo$_2$O$_4$ nanostructures have been investigated, including mesoporous nanosheets,[25] nanoneedle array,[26] and porous nanorod (NR) arrays/carbon fiber.[27] Although enhanced storage performance has been achieved, the electrochemical stability and cycling performance need further improvement by understanding the fundamental electrochemical conversion mechanism. In addition, the concomitant phase evolution still remains elusive. For example, by means of high-resolution X-ray photoelectron spectroscopy, Thissen et al.[28] claimed that the products after full sodiation are NiO and CoO, rather than the metallic Co and Ni that were confirmed by Alcántara et al. through ex situ X-ray diffraction.[24] Additionally, the desodiation process of NiCo$_2$O$_4$ electrode was

Dr. C. Y. Zhu, Prof. F. Xu, Dr. H. H. Min,
Dr. W. W. Xia, Prof. L. T. Sun
SEU-FEI Nano-Pico Center
Key Laboratory of MEMS of the Ministry of Education
Southeast University
Nanjing 210096, China
E-mail: fxu@seu.edu.cn; slt@seu.edu.cn
Dr. Y. Huang
Center for Functional Nanomaterials
Brookhaven National Laboratory
Upton, NY 11973, USA
Y. T. Wang, Prof. Q. Y. Xu
Department of Physics
Key Laboratory of MEMS of the Ministry of Education
Southeast University
Nanjing 210096, China
Prof. P. Gao
Electron Microscopy Laboratory
School of Physics
Center for Nanochemistry
Peking University
Beijing 100871, China
E-mail: p-gao@pku.edu.cn

DOI: 10.1002/adfm.201606163

**ADVANCED
SCIENCE NEWS**

www.advancedsciencenews.com

**ADVANCED
FUNCTIONAL
MATERIALS**

www.afm-journal.de

considered to proceed via the oxidation reaction of Co^0–Co^{3+} and Ni^0–Ni^{2+},[25,27] which apparently contradicted the recent work by Lee et al.,[26] who insisted that the desodiated products are CoO and NiO. Therefore, it is of great necessity to explore structural evolution and identify the underlying conversion mechanism of $NiCo_2O_4$ during sodiation–desodiation process.

In situ transmission electron microscopy (TEM) has been recognized as a powerful tool to real-time observe electrochemical reactions of electrode materials on the nanometer scale.[29–33] In this work, we constructed all-solid nanosized SIBs using individual $NiCo_2O_4$ NRs as working electrode inside a TEM, thus enabling direct visualization of structural and phase evolution of $NiCo_2O_4$ during the sodiation–desodiation cycling. A two-step phase transformation has been revealed during the first sodiation; intermediate-phase CoO and NiO were first formed, and then they are further converted into the Co and Ni nanograins embedded in Na_2O matrix. Upon the first desodiation, the desodiated products were not recovered to the original molecule of $NiCo_2O_4$, but evolved into divalent metal oxides of CoO and NiO. This result is different from the conversion reaction of $NiCo_2O_4$ material in LIBs. During subsequent sodiation–desodiation cycles, a reversible and symmetric phase transformation between CoO/Co and NiO/Ni was established. These findings, for the first time, identify the detailed sodiation–desodiation conversion mechanism of the $NiCo_2O_4$ material, shedding light on the mechanistic understanding extended to generic electrode materials for SIBs.

2. Results and Discussion

Crystal structure and morphology of as-prepared $NiCo_2O_4$ NRs are characterized in **Figure 1**. Figure 1a shows the X-ray diffraction (XRD) pattern, in which a series of distinct diffraction peaks are observed at 18.9°, 31.1°, 36.7°, 44.4°, and 59.0°, respectively. All of them can be indexed to the (111), (220), (311), (400), and (511) planes of the cubic spinel $NiCo_2O_4$ with lattice constants of $\alpha_0 = 0.8114$ nm (JCPDS, PDF no. 73-1702, space group $Fd3m$ (227)).[22] Morphology of the as-prepared $NiCo_2O_4$ is determined by scanning electron microscope (SEM) and TEM in Figure 1b,c, which presents NR-like structure with about 1 µm in length and 100 nm in diameter. Figure 1d gives an enlarged TEM image of an individual $NiCo_2O_4$ NR. Apparently, the $NiCo_2O_4$ NRs are composed of small $NiCo_2O_4$ nanoparticles with size of ≈10 nm. Such unique structure with abundant grain boundaries would augment the contact interface between the electrode and electrolyte, serving to facilitate the electron and sodium ions transport.[22] The inset in Figure 1d is the corresponding high-resolution TEM (HRTEM) image and the ordered lattice fringes of 0.46 nm match well with the (111) plane of $NiCo_2O_4$. Figure 1e further shows the electron diffraction (ED) pattern recorded from the $NiCo_2O_4$ NR. All diffraction rings confirm that the resultant products belong to the cubic spinel $NiCo_2O_4$ structure, where Ni^{2+} ions occupy the octahedral sites and Co^{3+} ions are distributed in both tetrahedral sites and octahedral sites,[22,23] as illustrated in Figure 1f.

To investigate the electrochemical behavior of $NiCo_2O_4$ during sodiation–desodiation cycles, an all-solid nanosized SIB that enables the in situ electrochemical experiments of an individual $NiCo_2O_4$ NR was constructed, as schematically shown in **Figure 2**a. Briefly, the nanosized electrochemical cell consists of a $NiCo_2O_4$ working electrode, a metal Na counter electrode on sharp tungsten probe, and a solid electrolyte of sodium oxide (Na_2O) layer naturally grown on the surface of metal Na. The
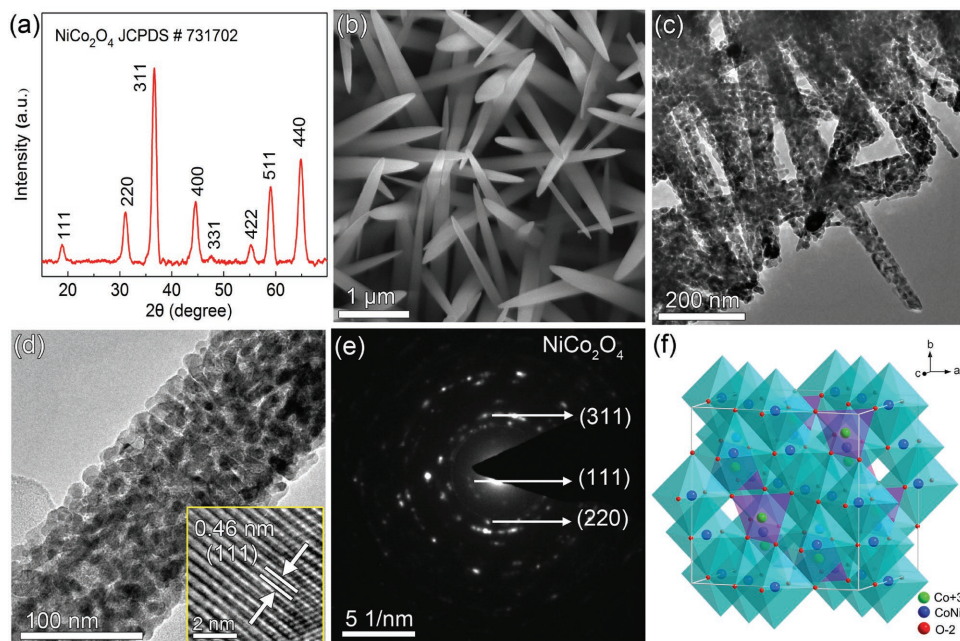
Figure 1. a) XRD pattern of the as-prepared $NiCo_2O_4$ NRs, corresponding to the cubic spinel structure. b) SEM and c) TEM images reveal the NR-like shape of $NiCo_2O_4$. d) Enlarged TEM image and e) the ED pattern of an individual $NiCo_2O_4$ NR, suggesting the NRs are assembled by $NiCo_2O_4$ nanoparticles. Inset in (d) shows the HRTEM image of $NiCo_2O_4$ NR with a typical lattice distance of 0.46 nm. f) Crystal structure of the cubic spinel $NiCo_2O_4$, where Ni^{2+} ions occupy the octahedral sites and Co^{3+} are distributed in both tetrahedral sites and octahedral sites.

ADVANCED
FUNCTIONAL
MATERIALS
www.afm-journal.de

ADVANCED
SCIENCE NEWS
www.advancedsciencenews.com
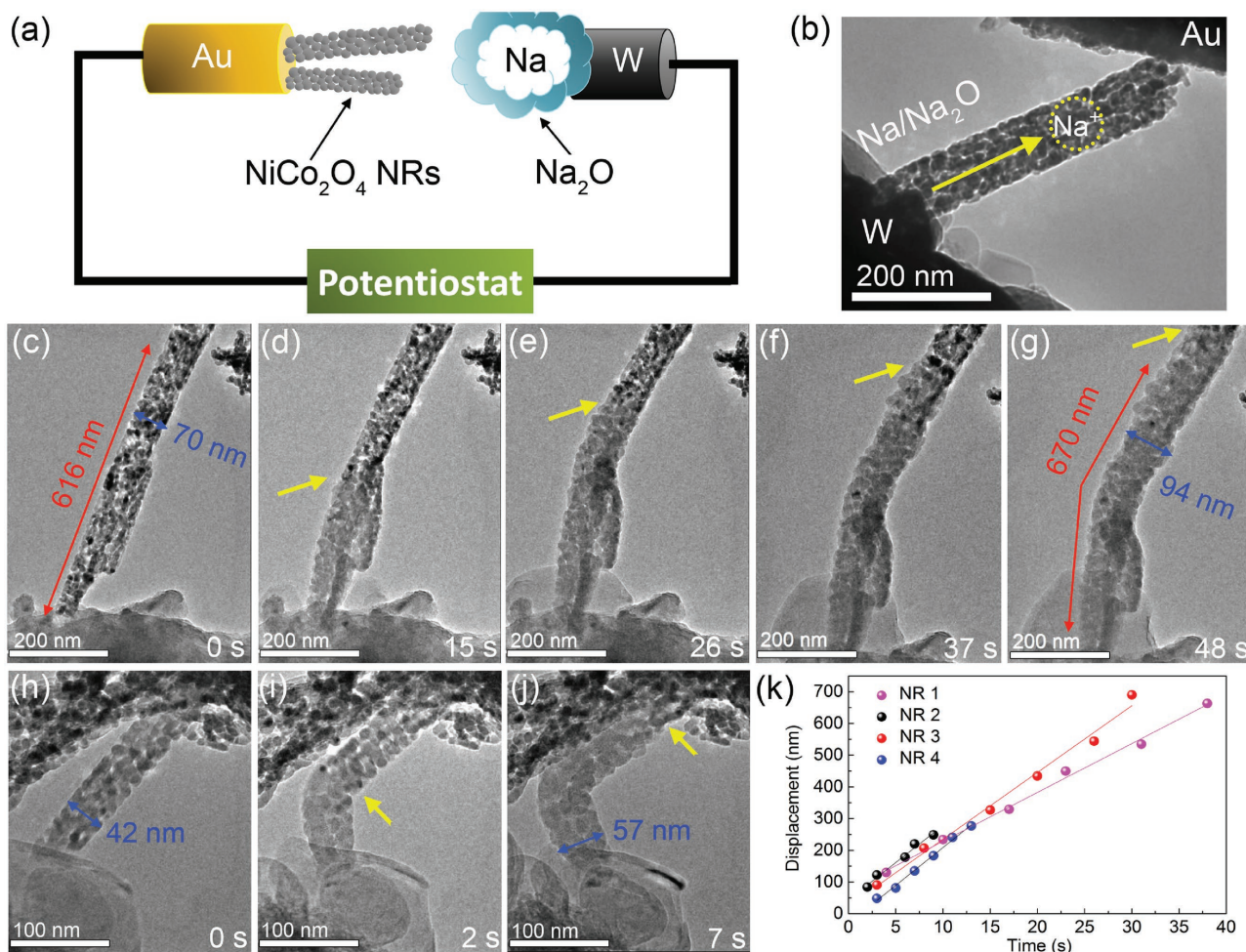
Figure 2. a) Schematic illustration of the experimental setup for in situ electrochemical sodiation–desodiation. b) A corresponding TEM image of the $NiCo_2O_4$ NR nanosized SIBs. c–j) The morphology evolution of two $NiCo_2O_4$ NRs during the first sodiation process. (c–g): NR 1; (h–j): NR 2. The yellow arrows denote the "sodiation reaction front." k) Relationship between the sodiation position and the sodiation time recorded from four $NiCo_2O_4$ NRs, showing homogeneous sodiation behaviors for $NiCo_2O_4$ NRs.

tungsten probe can be driven by a piezo-positioner inside TEM to make the Na/Na_2O layer and $NiCo_2O_4$ NRs in contact with each other by fine steps. Afterwards, constant potential was applied to the $NiCo_2O_4$ with respect to sodium, so as to drive the transport of sodium ions through the Na_2O layer, consequently initiating the electrochemical sodiation–desodiation process. Figure 2b gives the corresponding TEM image of the nanosized SIBs using $NiCo_2O_4$ NR as electrode material. The yellow arrow denotes the direction of the transport of sodium ions.

Figures 2c–g and 2h–j present the time-sequence TEM images of two $NiCo_2O_4$ NRs (named as NR 1 and NR 2) during the first sodiation process, and the morphological and structural evolutions have been observed (Movies S1 and S2, Supporting Information). Before sodiation, the diameter of pristine $NiCo_2O_4$ NRs is ≈70 and 42 nm for NR 1 and NR 2, respectively. When a potential of −1.5 V was applied to the $NiCo_2O_4$ with respect to sodium, sodium ions began to diffuse from one side of the NR that was in contact with the Na/Na_2O layer and gradually propagated to the other side. Such a sodiation process

can be visualized by the "sodiation reaction front" (marked with yellow arrows) through the distinct contrast between the sodiated and unsodiated regions. To probe the sodium ion transport dynamics in $NiCo_2O_4$ NRs, the reaction front displacement of four NRs as a function of time is plotted in Figure 2k. All curves are featured by the linear correlation, indicating that the $NiCo_2O_4$ NRs possess homogeneous sodiation behaviors. The corresponding sodiation migration rates were then measured to be as high as 15–24 nm s^{-1}. Different reaction rates are possibly attributed to the difference between the electrodes contact and the local Na^+ concentration.[32] The linear correlation with high slope between the sodiation migration and time is likely ascribed to the unique nanoparticle-based NR structure providing abundant grain boundaries. It is reported that grain boundaries have a lower lithium/sodium-ion diffusion barrier and provide a faster lithium/sodium-ion diffusion pathway.[31,34,35] In addition, the grain boundaries are weak in shear and cleavage, which make the Co—O and Ni—O bonds easily broken under the strain caused by sodiation. Accordingly, the fast sodiation reaction of the surface grains led to the

ADVANCED
SCIENCE NEWS
www.advancedsciencenews.com

ADVANCED
FUNCTIONAL
MATERIALS
www.afm-journal.de
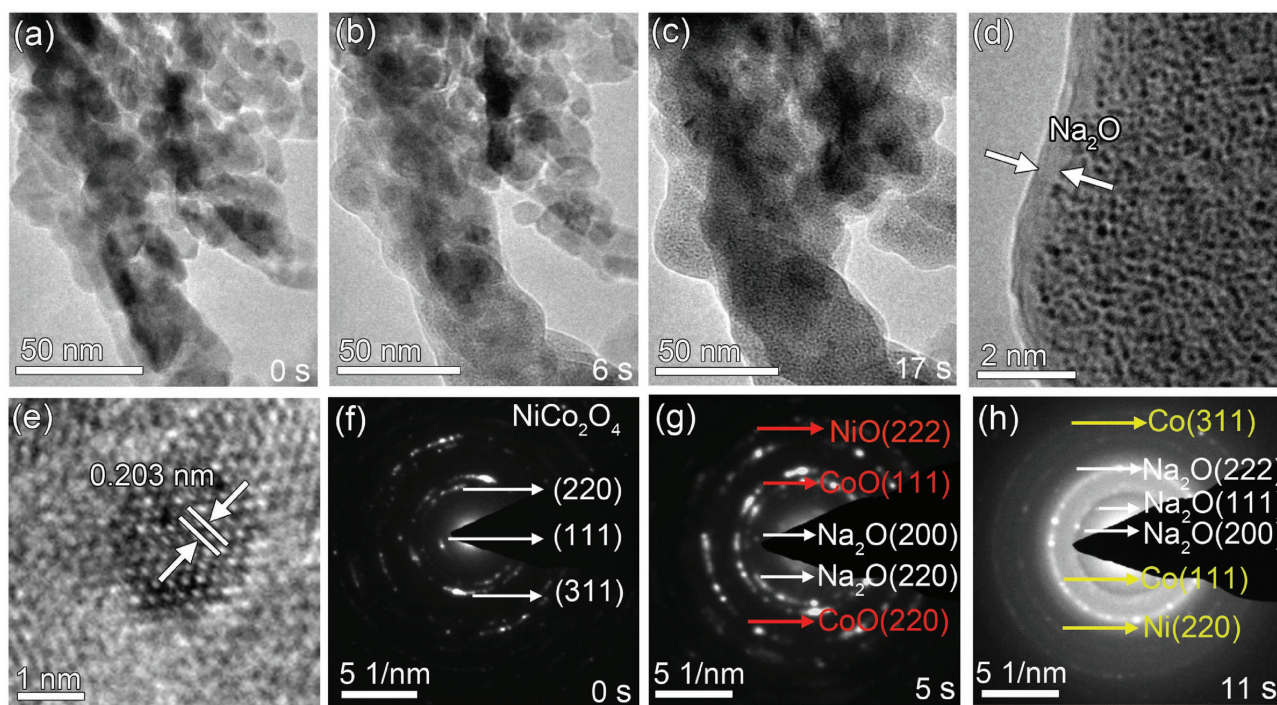
Figure 3. a–c) Microstructural evolution of a segment of $NiCo_2O_4$ NR during the first sodiation process. d) Enlarged TEM and e) HRTEM image of the sodiated product. f–h) Time-lapsed ED patterns for the initial $NiCo_2O_4$, and intermediate and final sodiation products, revealing the two-step phase evolution of $NiCo_2O_4$ NR during the first electrochemical sodiation.

bending of NRs with limited space between the Au and sodium electrodes. This phenomenon has also been observed in SnO_2 nanowire and MoO_3 nanobelt.[31,32] After full sodiation, the two NRs show the same radial expansion of ≈35%. Meanwhile, the axial elongation is estimated to be ≈9% (Figure 2c–g) and the volume expansion of the NRs can therefore be calculated to be ≈100%. No visible crack and fracture are observed in fully sodiated $NiCo_2O_4$, indicating a reliable structural evolution.

More detailed structural and phase evolution of $NiCo_2O_4$ NRs during the first sodiation were tracked by HRTEM and ED (**Figure 3**; Movie S3, Supporting Information). The fully sodiated product is featured by the ultrafine nanograins and a thin layer with a thickness of ≈6 nm was formed on the surface of the NR (Figure 3a–d). The corresponding HRTEM image in Figure 3e clearly shows a newly formed nanograin. Upon initial sodiation, the diffraction spots of $NiCo_2O_4$ disappeared completely, whereas distinct diffraction rings corresponding to the crystalline Na_2O (JCPDS, PDF no. 03-1074) were detected (Figure 3g); moreover, NiO and CoO phases were also observed as intermediate products. This indicates that sodium ions have been inserted into the host structure of $NiCo_2O_4$ and sodiation reaction occurred. Upon full sodiation, the diffraction rings of NiO and CoO vanished, while metallic Co, Ni, and Na_2O are detected as the fully sodiated products (Figure 3h). Generally, NiO and Ni would generate first during the sodiation compared with CoO and Co, as nickel has higher electrochemical platform than cobalt. However, we have not captured these distinctions with in situ ED patterns within such a fast reaction time. Consequently, a two-step conversion reaction mechanism for $NiCo_2O_4$ during the first sodiation is revealed as follows:

$$NiCo_2O_4 + 2Na^+ + 2e^- \rightarrow NiO + 2CoO + Na_2O \tag{1}$$

$$NiO + 2Na^+ + 2e^- \rightarrow Ni + Na_2O \tag{2}$$

$$CoO + 2Na^+ + 2e^- \rightarrow Co + Na_2O \tag{3}$$
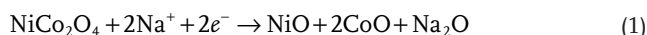
For the first desodiation, a positive potential of 3 V was applied to extract sodium ions from the sodiated NR. The morphology evolution is displayed in the **Figure 4**a–f and Movie S4 (Supporting Information). With the extraction of sodium ions, the diameter of the sodiated NR gradually shrunk from 41 to 27 nm within 45 s, resulting in a contraction of 33%. The Na_2O layer on the surface of the NR also vanished. Figure 4g displays the HRTEM image of the desodiated NR and ordered lattice fringes correspond to the crystallized desodiated products. The ED patterns were used to identify the crystallized desodiated products (Figure 4h). As expected, diffraction rings of Co and Ni phases disappeared, whereas the CoO and NiO phases can be detected. Moreover, Na_2O phase was also detected by the vague diffraction rings. These results indicate that the metallic Co and Ni evolved into divalent metal oxides of CoO and NiO rather than the initial $NiCo_2O_4$ upon the first full desodiation. Such irreversible phase conversion has been widely observed in conversion reactions of transition metal oxides during the first sodiation/desodiation or lithiation/delithiation, such as Fe_2O_3, Co_3O_4, $ZnFe_2O_4$, and MoO_3.[32,36–39] It is generally accepted that the electrochemically driven size confinement of metal particles can greatly enhance their electrochemical activity toward the formation/decomposition of Na_2O or Li_2O.[36,37,40] In our

ADVANCED
FUNCTIONAL
MATERIALS
www.afm-journal.de

ADVANCED
SCIENCE NEWS
www.advancedsciencenews.com
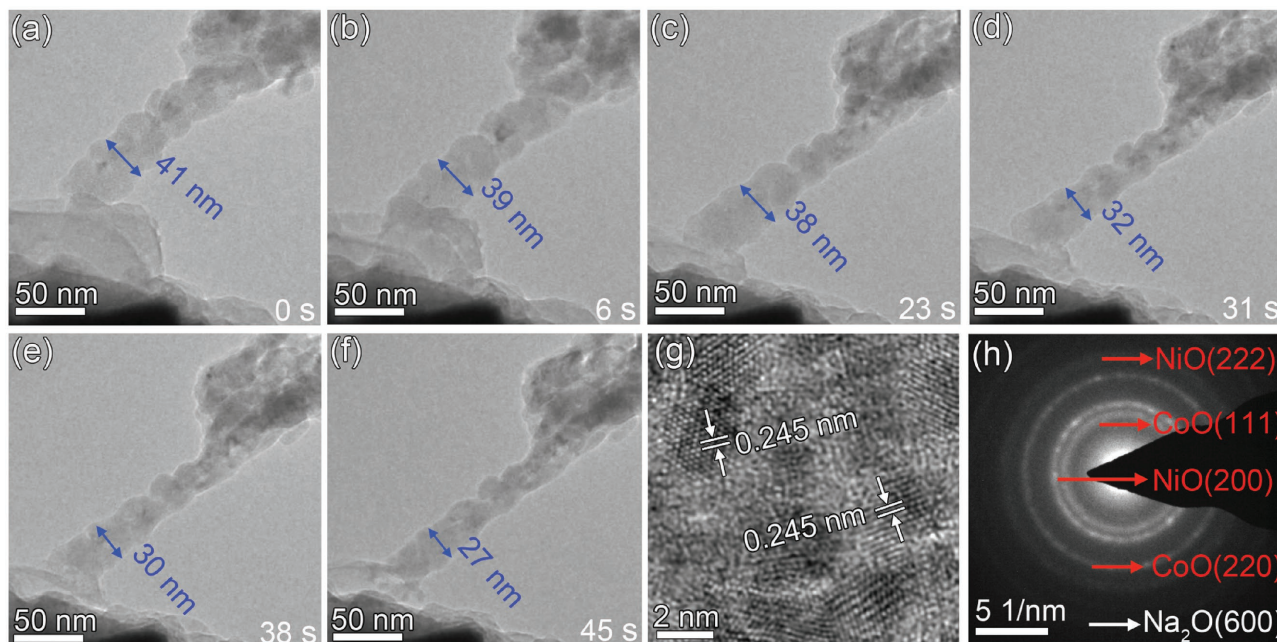
Figure 4. a–f) Microstructure evolutions of a segment of NiCo$_2$O$_4$ NR during the first desodiation. g) HRTEM image and h) ED pattern of the fully desodiated NR.

work, the decomposition of Na$_2$O during the desodiation could be attributed to the electrocatalysis of the ultrafine Co and Ni nanograins. As the desodiation reaction proceeded, CoO and NiO nanograins gradually formed. The electrocatalytic activity of monoxide CoO and NiO materials is much weaker as compared to that of Co and Ni nanograins,[37,40] thus the electrochemical reaction would cease after full conversion of Co and Ni into CoO and NiO. That is the reason why the sodiated products cannot be recovered to the initial NiCo$_2$O$_4$ phase. The conversion reactions during the first desodiation can be expressed as

$$Co + Na_2O \rightarrow CoO + 2Na^+ + 2e^- \tag{4}$$

$$Ni + Na_2O \rightarrow NiO + 2Na^+ + 2e^- \tag{5}$$
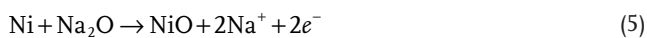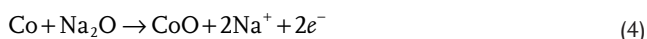
Thus, the irreversible reaction should be responsible for the huge capacity loss that plagues the first sodiation–desodiation cycle in SIBs.

To identify the overall electrochemical conversion mechanism of NiCo$_2$O$_4$, cycling performance was subsequently investigated for another NiCo$_2$O$_4$ NR (**Figure 5**a–g; Movie S5, Supporting Information). Interestingly, the NR exhibited multicycle reversible volume expansion and contraction with the insertion and extraction of sodium ions, demonstrating that the NiCo$_2$O$_4$ material is viable for the recyclable SIBs. Figure 5h further displays the specific expansion and contraction rates for each electrochemical sodiation–desodiation cycle. The expansion rates of the following sodiation processes are lower than that of the first sodiation, suggesting a different conversion mechanism during the following sodiation–desodiation cycles.[36] Accordingly, the ED patterns for the first two sodiation–desodiation cycles are acquired in Figure 5i–l. It can be seen that the first fully

sodiated products are metal Co, Ni, and Na$_2$O (Figure 5i), which further converted into CoO and NiO (Figure 5j) as the first desodiated products. This result is consistent with the above observation. Although the starting material during the second sodiation was different from that in the first sodiation, the sodiated product was the same as the first sodiated one (i.e., Co and Ni; Figure 5k). Moreover, the ED pattern of the second desodiated products in Figure 5l also exhibited the same characteristic with that of the first desodiated products (Figure 5j). This indicates that although the asymmetric conversion reactions occurred during the first sodiation–desodiation, the subsequent electrochemical cycles are reversible between the CoO/Co and NiO/Ni phases, as illustrated in **Figure 6**. Considering that the electron beam could affect the sodiation/desodiation behavior, we further conducted a control experiment on the NiCo$_2$O$_4$ NR with the electron beam off. Only when we collected ED patterns, the electron beam was turned on for several seconds. The structural evolutions observed during the whole sodiation/desodiation (Figure S1, Supporting Information) are consistent with the observations with the electron beam irradiation, implying that the electron beam irradiation did not affect the identification of phase transformation.

To correlate the macroscopic electrochemical properties of NiCo$_2$O$_4$ NRs with the microcosmic in situ TEM observations, electrochemical characterizations were performed on NiCo$_2$O$_4$ NR-based coin-type half cells. From Figure S2 (Supporting Information), two distinct plateau regions (denoted by A$_1$ and A$_2$) were observed for the first sodiation reaction of NiCo$_2$O$_4$ at ≈0.6 V versus Na/Na$^+$ and ≈0.1 V versus Na/Na$^+$, respectively. Based on the in situ TEM results, the A$_1$ plateau region can be ascribed to the reduction of NiCo$_2$O$_4$ to CoO and NiO while the A$_2$ plateau is due to the further conversion to Co and Ni. Figure S3 (Supporting Information) further shows the galvanostatic cycling

**ADVANCED
SCIENCE NEWS**
www.advancedsciencenews.com

**ADVANCED
FUNCTIONAL
MATERIALS**
www.afm-journal.de
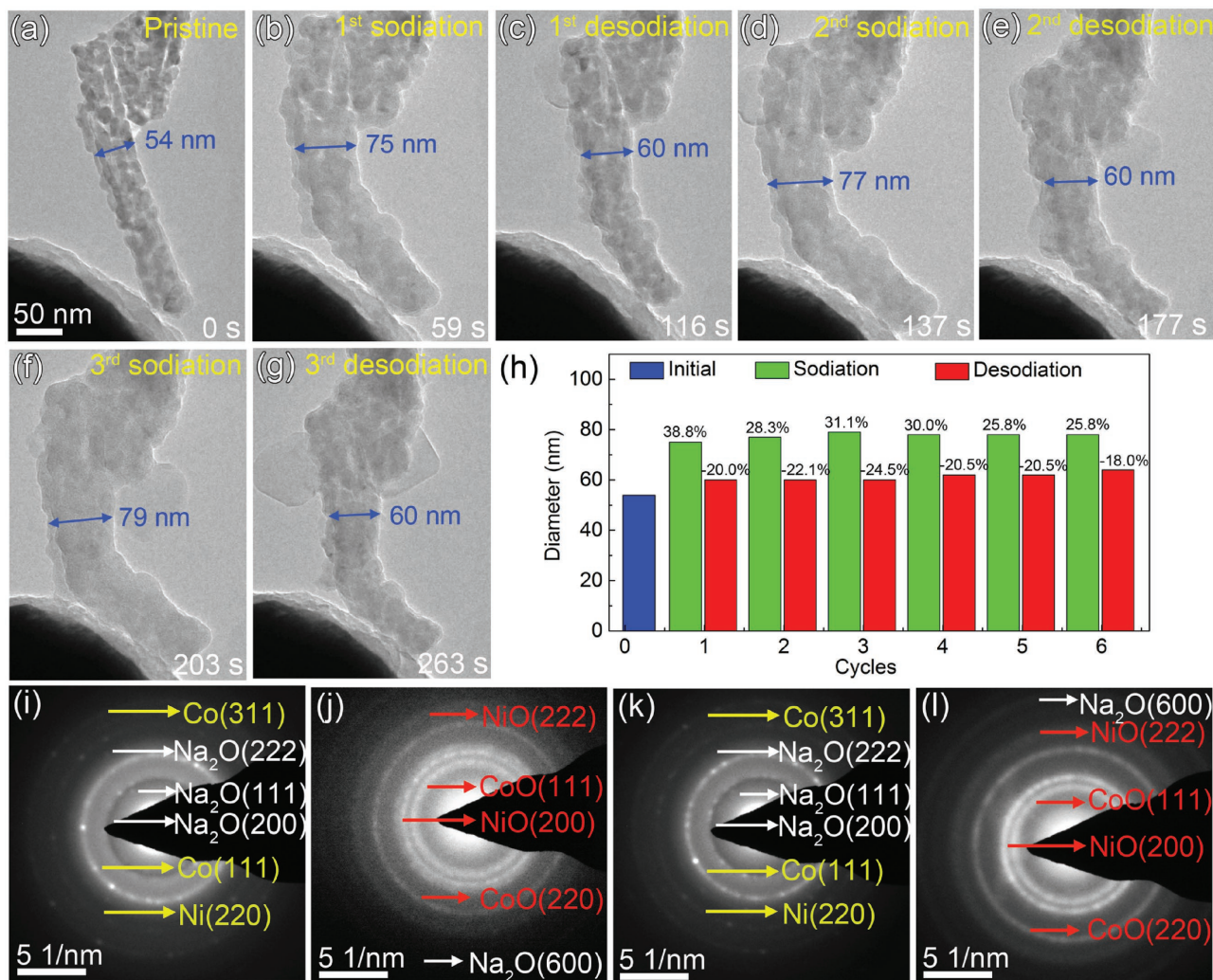
Figure 5. a–g) Microstructure evolutions of NiCo$_2$O$_4$ NR in the first three electrochemical sodiation–desodiation processes. h) The measured diameters versus electrochemical cycling times of the NiCo$_2$O$_4$. The numeric percentages are for the diameter expansion/contraction during each event. i–l) ED patterns of the first (i–j) and the second (k–l) sodiation–desodiation products to identify the overall reaction mechanism of NiCo$_2$O$_4$ in SIBs.

performance of NiCo$_2$O$_4$. It delivers an initial discharge capacity of 552 mAh g^{-1} and charge capacity of 256 mAh g^{-1} with Coulombic efficiency of 46.3%. The initial discharge capacity is lower than theoretical capacity of 889 mAh g^{-1}, which is likely attributed to the formation of solid electrolyte interphase (SEI) film and the incomplete reduction of NiCo$_2$O$_4$ caused by electrolyte decomposition, metal Na deposition, and some other packaging process.[36,41,42] After the first electrochemical cycle, obvious capacity fading of 279 mAh g^{-1} is found for NiCo$_2$O$_4$-based SIBs. Combining the in situ TEM analysis, the irreversible phase conversion (889 mAh g^{-1} for NiCo$_2$O$_4$ and 715 mAh g^{-1} for CoO or NiO) accounts for around 62% of the total capacity loss of NiCo$_2$O$_4$ electrode; about 38% of the capacity loss can be caused by other irreversible electrochemical processes, such as the formation of an SEI layer.[37] In subsequent electrochemical cycles, the discharge/charge capacities tend to be stable with a Coulombic efficiency of >93%. This result agrees well with in situ TEM observations that NiCo$_2$O$_4$ NRs show an irreversible phase change during the first cycle but are recyclable in the following cycles.

3. Conclusion

In conclusion, the conversion-type electrode material of spinel NiCo$_2$O$_4$ has been investigated by using in situ TEM to probe its structural and phase evolutions in real time during electrochemical sodiation–desodiation cycling. A two-step phase transformation has been identified during the first sodiation of NiCo$_2$O$_4$. Intermediate phases of CoO and NiO were first generated, followed by further transformation into Co and Ni nanograins embedded in Na$_2$O matrix. During the first desodiation, Co and Ni phases were converted into divalent metal oxides CoO and NiO, rather than the original molecule of NiCo$_2$O$_4$, indicating an asymmetric conversion reaction mechanism. This result is different from the conversion mechanism of NiCo$_2$O$_4$ material in LIBs and should be responsible for the inferior storage performance in SIBs. Impressively, a stable and reversible phase transformation was established between CoO/NiO and Co/Ni during subsequent electrochemical cycles. These findings, for the first time, identify the detailed

**ADVANCED
FUNCTIONAL
MATERIALS**

www.afm-journal.de

**ADVANCED
SCIENCE NEWS**

www.advancedsciencenews.com
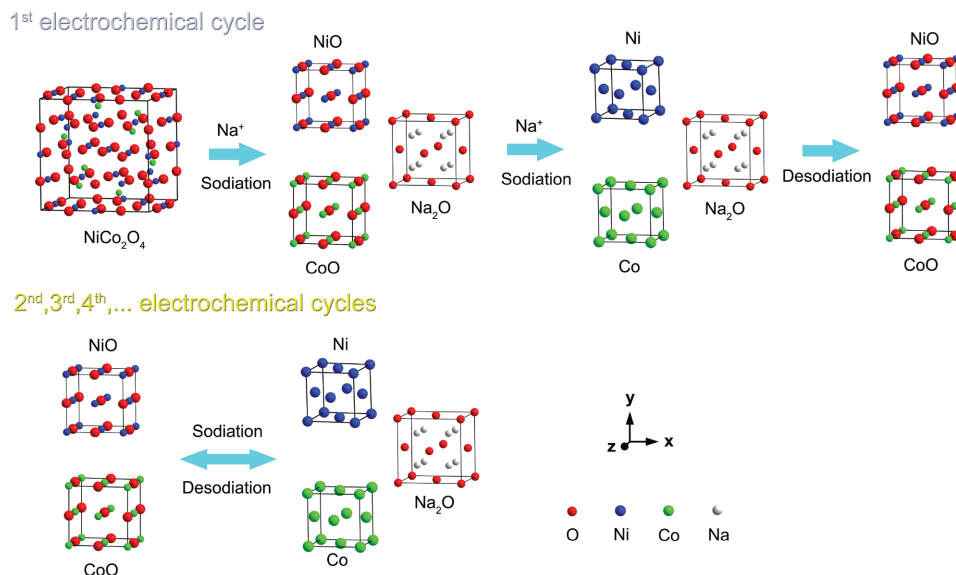
Figure 6. Schematic illustration of the conversion mechanism of the $NiCo_2O_4$ material during its first and subsequent electrochemical sodiation–deso-diation cycles.

sodiation–desodiation conversion mechanism of the $NiCo_2O_4$ material, shedding light on the mechanistic understanding extended to generic electrode materials for SIBs.

potential was then applied to the $NiCo_2O_4$ NRs with respect to sodium counter electrode to drive the transport of sodium ions through the solid-state electrolyte Na_2O layer, thereby initiating the electrochemical sodiation–desodiation process.

4. Experimental Section

Preparation of $NiCo_2O_4$ NRs: $NiCo_2O_4$ NRs were synthesized by a hydrothermal method. Briefly, Ffuorine-doped tin oxide (FTO) conducting substrate was first washed with ethanol and deionized water and then put into the sealed Teflon-lined stainless steel autoclave, in which $Co(NO_3)_2 \cdot 6\ H_2O$ (1.16 g, 4×10^{-3} M), $Ni(NO_3)_2 \cdot 6\ H_2O$ (0.58 g, 2×10^{-3} M), and urea (0.6 g, 10×10^{-3} M) were dissolved in aqueous solution (40 mL). The sealed autoclave was subsequently heated at 120 °C for 10 h to form metallic carbonate hydroxide precursors on the FTO substrate. After reaction, the FTO was rinsed by deionized water and ethanol, and then annealed under N_2 atmosphere at 350 °C for 2 h. The bimetallic carbonate hydroxide products were gradually converted into bimetallic oxides ($NiCo_2O_4$). Finally, the obtained $NiCo_2O_4$ NRs are scraped by blade for experiments.

Characterization: Phase identification and surface morphology of $NiCo_2O_4$ were characterized by powder X-ray diffractometer (ARLXTRA, Thermo Electron Co., USA) with Cu Kα radiation as the X-ray source, and scanning electron microscope (JSM-7600F, JEOL, Japan) operated at 15 kV. Further structural analyses were carried out by transmission electron microscope (FEI Titan 80-300) at 300 kV.

In Situ Electrochemical Experiments: A high-resolution transmission electron microscope (FEI Titan 80-300) is used for the in situ observation of the electrochemical behaviors of $NiCo_2O_4$ NRs during the electrochemical sodiation–desodiation process, with the assistance of ED pattern and HRTEM imaging. To prepare the nanosized SIBs, $NiCo_2O_4$ NRs were attached to Au wire as working electrode. Bulk sodium metal was scratched on a sharp tungsten (W) tip and then served as counter electrode. Further, a layer of Na_2O, grown on the surface of metal Na due to the exposure to air during the loading process of the TEM holder, can be used as the solid electrolyte for sodium ion transport. During the experiments, the TEM holder was quickly transferred into the TEM chamber. The tungsten probe was driven by a piezo-positioner inside TEM to make the Na/Na_2O and $NiCo_2O_4$ NRs contact with each other. A constant negative/positive

Supporting Information

Supporting Information is available from the Wiley Online Library or from the author.

Acknowledgements

[1] B. Dunn, H. Kamath, J. M. Tarascon, *Science* **2011**, *334*, 928.

[2] M. Armand, J. M. Tarascon, *Nature* **2008**, *451*, 652.

[3] C. D. Wessells, S. V. Peddada, R. A. Huggins, Y. Cui, *Nano Lett.* **2011**, *11*, 5421.

[4] P. G. Bruce, S. A. Freunberger, L. J. Hardwick, J. M. Tarascon, *Nat. Mater.* **2012**, *11*, 19.

[5] C. Y. Wang, G. S. Zhang, S. H. Ge, T. Xu, Y. Ji, X. G. Yang, Y. J. Leng, *Nature* **2016**, *529*, 515.

[6] D. Kundu, E. Talaie, V. Duffort, L. F. Nazar, *Angew. Chem., Int. Ed.* **2015**, *54*, 3431.

[7] C. Fang, Y. H. Huang, W. X. Zhang, J. T. Han, Z. Deng, Y. L. Cao, H. X. Yang, *Adv. Energy Mater.* **2016**, *6*, 1501727.

**ADVANCED
SCIENCE NEWS**

www.advancedsciencenews.com

**ADVANCED
FUNCTIONAL
MATERIALS**

www.afm-journal.de

[8] M. D. Slater, D. H. Kim, E. Lee, C. S. Johnson, *Adv. Funct. Mater.* **2013**, *23*, 947.

[9] Y. J. Zhu, Y. Wen, X. L. Fan, T. Gao, F. D. Han, C. Luo, S. C. Liou, C. S. Wang, *ACS Nano* **2015**, *9*, 3254.

[10] L. Wu, X. H. Hu, J. F. Qian, F. Pei, F. Y. Wu, R. J. Mao, X. P. Ai, H. X. Yang, Y. L. Cao, *Energy Environ. Sci.* **2014**, *7*, 323.

[11] Y. C. Liu, N. Zhang, L. F. Jiao, Z. L. Tao, J. Chen, *Adv. Funct. Mater.* **2015**, *25*, 214.

[12] X. L. Fan, J. F. Mao, Y. J. Zhu, C. Luo, L. M. Suo, T. Gao, F. D. Han, S. Liou, C. S. Wang, *Adv. Energy Mater.* **2015**, *5*, 1500174.

[13] M. T. Sougrati, A. Darwiche, X. H. Liu, A. Mahmoud, R. P. Hermann, S. Jouen, L. Monconduit, R. Dronskowski, L. Stievano, *Angew. Chem., Int. Ed.* **2016**, *55*, 5090.

[14] Y. F. Yuan, L. Ma, K. He, W. T. Yao, A. Nie, X. X. Bi, K. Amine, T. Wu, J. Lu, R. Shahbazian-Yassr, *Nano Energy* **2016**, *19*, 382.

[15] Q. M. Su, G. H. Du, J. Zhang, Y. J. Zhong, B. S. Xu, Y. H. Yang, S. Neupane, W. Z. Li, *ACS Nano* **2014**, *8*, 3620.

[16] J. Barker, M. Y. Saidi, J. L. Swoyer, *Electrochem. Solid-State Lett.* **2003**, *6*, A1.

[17] S. W. Kim, D. H. Seo, X. Ma, G. Ceder, K. Kang, *Adv. Energy Mater.* **2012**, *2*, 710.

[18] K. He, Y. N. Zhou, P. Gao, L. P. Wang, N. Pereira, G. G. Amatucci, K. W. Nam, X. Q. Yang, Y. M. Zhu, F. Wang, D. Su, *ACS Nano* **2014**, *8*, 7251.

[19] C. Z. Yuan, H. B. Wu, Y. Xie, X. W. Lou, *Angew. Chem., Int. Ed.* **2014**, *53*, 1488.

[20] G. Zhang, L. Yu, H. B. Wu, H. E. Hoster, X. W. Lou, *Adv. Mater.* **2012**, *24*, 4609.

[21] P. F. Teh, Y. Sharma, S. S. Pramana, M. Srinivasan, *J. Mater. Chem.* **2011**, *21*, 14999.

[22] B. S. Li, J. K. Feng, Y. T. Qian, S. L. Xiong, *J. Mater. Chem. A* **2015**, *3*, 10336.

[23] J. F. Li, S. L. Xiong, Y. R. Liu, Z. C. Ju, Y. T. Qian, *ACS Appl. Mater. Interfaces* **2013**, *5*, 981.

[24] R. Alcántara, M. Jaraba, P. Lavela, J. L. Tirado, *Chem. Mater.* **2002**, *14*, 2847.

[25] K. Q. Zhou, Z. S. Hong, C. B. Xie, H. Dai, Z. G. Huang, *J. Alloys Compd.* **2015**, *651*, 24.

[26] J. W. Lee, H. S. Shin, C. W. Lee, K. N. Jung, *Nanoscale Res. Lett.* **2016**, *11*, 1.

[27] Y. D. Mo, Q. Ru, J. F. Chen, X. Song, L. Y. Guo, S. J. Hu, S. M. Penge, *J. Mater. Chem. A* **2015**, *3*, 19765.

[28] A. Thissen, D. Ensling, F. J. F. Madrigal, W. Jaegermann, *Chem. Mater.* **2005**, *17*, 5202.

[29] J. Y. Huang, L. Zhong, C. M. Wang, J. P. Sullivan, W. Xu, L. Q. Zhang, S. X. Mao, N. S. Hudak, X. H. Liu, *Science* **2010**, *330*, 1515.

[30] M. T. McDowell, I. Ryu, S. W. Lee, C. M. Wang, W. D. Nix, Y. Cui, *Adv. Mater.* **2012**, *24*, 6034.

[31] M. Gu, A. Kushima, Y. Y. Shao, J. G. Zhang, J. Liu, N. D. Browning, J. Li, C. M. Wang, *Nano Lett.* **2013**, *13*, 5203.

[32] W. W. Xia, Q. B. Zhang, F. Xu, L. T. Sun, *ACS Appl. Mater. Interfaces* **2016**, *8*, 9170.

[33] F. Xu, Z. R. Li, L. J. Wu, Q. P. Meng, H. L. L. Xin, J. Sun, B. H. Ge, L. T. Sun, Y. M. Zhu, *Nano Energy* **2016**, *30*, 771.

[34] X. Zhu, C. S. Ong, X. Xu, B. Hu, J. Shang, H. Yang, S. Katlakunta, Y. Liu, X. Chen, L. Pan, J. Ding, R. W. Li, *Sci. Rep.* **2013**, *3*, 1084.

[35] H. Paul, I. Sylvio, *J. Phys.: Condens. Matter* **2003**, *15*, R1257.

[36] W. W. Xia, F. Xu, C. Y. Zhu, H. L. L. Xin, Q. Y. Xu, P. P. Sun, L. T. Sun, *Nano Energy* **2016**, *27*, 447.

[37] Q. M. Su, D. Xie, J. Zhang, G. H. Du, B. S. Xu, *ACS Nano* **2013**, *7*, 9115.

[38] Q. M. Su, S. X. Wang, L. B. Yao, H. J. Li, G. H. Du, H. Q. Ye, Y. Z. Fang, *Sci. Rep.* **2016**, *6*, 28197.

[39] Q. M. Su, J. Zhang, Y. S. Wu, G. H. Dun, *Nano Energy* **2014**, *9*, 264.

[40] P. Poizot, S. Laruelle, S. Grugeon, L. Dupont, J. M. Tarascon, *Nature* **2000**, *407*, 496.

[41] Z. Li,, J. Huang, B. Y. Liaw, V. Metzler, J. B. Zhang, *J. Power Sources* **2014**, *254*, 168

[42] J. M. Tarascon, M. Armand, *Nature* **2001**, *414*, 359.

FULL PAPER